Nanostructured Electrode Enabling Fast and Fully Reversible MnO2 -to-Mn2+ Conversion in Mild Buffered Aqueous Electrolytes

Mickaël Mateos, Kenneth R. Harris, Benoit Limoges, Veronique Balland

Nanostructured electrode enabling fast and fully-reversible MnO_2-to-Mn^{2+} conversion in mild buffered aqueous electrolytes

Mickaël Mateos [†], *Kenneth D. Harris* [‡,§], *Benoît Limoges* [†,*], *Véronique Balland* [†,*]

[†] Laboratoire d'Electrochimie Moléculaire, Université de Paris, UMR CNRS 7591, 15 rue Jean-Antoine de Baïf, Paris F-75205 cedex 13, France.

[‡] National Research Council Canada, Nanotechnology Research Centre, Edmonton, Alberta, T6G 2M9, Canada

[§] Department of Mechanical Engineering, University of Alberta, Edmonton, Alberta, T6G 2V4, Canada

Keywords: manganese dioxide, rechargeable aqueous batteries, conversion reaction, proton-coupled electron transfer, electrodeposition

Abstract

On account of their low-cost, earth abundance, eco-sustainability, and high theoretical charge storage capacity, MnO_2 cathodes have attracted a renewed interest in the development of rechargeable aqueous batteries. However, they currently suffer from limited gravimetric capacities when operating under the preferred mild aqueous conditions, which leads to lower performance as compared to similar devices operating in strongly acidic or basic conditions. Here, we demonstrate how to overcome this limitation by combining a well-defined 3D nanostructured conductive electrode, which ensures an efficient reversible MnO_2-to-Mn^{2+} conversion reaction, with a mild acid buffered electrolyte (pH 5). A reversible gravimetric capacity of 560 $mA \cdot h \cdot g^{-1}$ (close to the maximal theoretical capacity of 574 $mA \cdot h \cdot g^{-1}$ estimated from the MnO_2 average oxidation state of 3.86) was obtained over rates ranging from 1 to 10 $A \cdot g^{-1}$. The rate capability was also remarkable, demonstrating a capacity retention of 435 $mA \cdot h \cdot g^{-1}$ at a rate of 110 $A \cdot g^{-1}$. These good performances have been attributed to optimal regulation of the mass transport and electronic transfer between the three process actors, *i.e.* the 3D conductive scaffold, the MnO_2 active material filling it, and the soluble species involved in the reversible conversion reaction. Additionally, the high reversibility and cycling stability of this conversion reaction is demonstrated over 900 cycles with a Coulombic efficiency > 99.4 % at a rate of 44 $A \cdot g^{-1}$. Besides these good performances, also demonstrated in a Zn/MnO_2 cell configuration, we discuss the key parameters governing the efficiency of the MnO_2-to-Mn^{2+} conversion. Overall, the present study provides a comprehensive framework for the rational design and optimization of MnO_2 cathodes involved in rechargeable mild aqueous batteries.

Introduction

The development of rechargeable aqueous batteries for large-scale electrochemical energy storage devices is driven by their ability to achieve appropriate energy densities with safe, sustainable and inexpensive chemicals.[1,2] Among the different aqueous batteries, the rechargeable Zn/MnO_2 battery, able to operate in a mild aqueous electrolyte, is certainly the most attractive, especially since the breakthrough of Pan *et al*. in 2016,[3] who demonstrated a high reversibility and excellent cycling stability when using a mild acidic electrolyte containing both $ZnSO_4$ and $MnSO_4$. Since then, the concept has been explored in many studies, varying the nature of the MnO_2 cathode and the chemical composition of the Zn^{2+}-based aqueous electrolyte.[4] Despite all these efforts, however, the gravimetric capacities of mild aqueous Zn/MnO_2 batteries remain capped to 350-380 $mA{\cdot}h{\cdot}g^{-1}$,[4–6] which is far from the maximal theoretical value of 617 $mA{\cdot}h{\cdot}g^{-1}$ associated with the reversible 2-electron reduction of Mn(IV) into Mn(II).

Recently, we have revealed that the charge storage mechanism at MnO_2 electrodes is not based on an insertion process but instead on a reversible conversion principle, wherein the weak Brønsted acid AH and conjugated base A^- present in an aqueous buffered electrolyte assist the following proton-coupled electron transfer reaction at the electrode interface:[7]

$$MnO_{2(s)} + 4\ AH + 2\ e^- \leftrightarrows Mn^{2+}_{(aq)} + 4\ A^- + 2\ H_2O \qquad (1)$$

According to this reaction, the 2-electron gravimetric capacity of MnO_2 should be accessible in a mild, non-corrosive buffered aqueous media, which according to the Pourbaix diagram lies within the domain of thermodynamic stability of Mn^{2+}.[8] In our previous work, the maximal gravimetric capacity achieved in a buffered electrolyte of pH 5 was 450 $mA{\cdot}h{\cdot}g^{-1}$ (obtained from MnO_2 thin films electrodeposited onto planar electrodes).[7] Although much better than the

capacities previously reported for a range of MnO_2-cathodes in mild unbuffered aqueous electrolytes, this gravimetric capacity remains far from the 570 $mA \cdot h \cdot g^{-1}$ value recently achieved in a strongly acidic electrolyte (*i.e.*, 0.1 M H_2SO_4).[9] In this case, a similar conversion reaction is at work, but with H_3O^+/H_2O acting as the proton donor/acceptor couple. Further studies are thus required to better understand the key factors and parameters currently limiting the MnO_2-to-Mn^{2+} conversion in mild aqueous electrolytes. Our previous work leads us to believe that two issues are critical: (*i*) the efficiency of the electrical wiring between the MnO_2 solid phase and the underlying current collector, and (*ii*) the appropriate regulation of both the electron transport/transfer at the electrode/MnO_2 film/electrolyte interface and the mass transport of all soluble species involved in reaction 1 (*i.e.*, Mn^{2+}, AH, and A^-).[10] Indeed, if misbalanced, the Coulombic efficiency (*CE*) lies below 100 %, inducing a progressive decrease of the electrode gravimetric capacity upon cycling because of the incomplete exploitation of MnO_2.[7]

Concerning the electron transfer between the semi-conductive MnO_2 and the current collector, a few studies have reported on the poor adhesion and mechanical stability of MnO_2 on conductive substrates of various chemical composition and roughness.[11,12] Furthermore, because of the moderate electronic conductivity (10^{-3}-10^{-4} $S \cdot cm^{-1}$) of MnO_2,[13,14] the ohmic drop is expected to rise together with the film thickness. All these issues can potentially be solved by using a 3D nanostructured current collector, with a high aspect ratio, well-suited for the conformal electrodeposition of thin films of MnO_2 to provide shorter ion diffusion distances and better electron harvesting paths.[10,15] Previously, such a strategy has been successfully exploited to improve the performances of MnO_2-based supercapacitors,[16–18] as well as MnO_2 cathodes toward reversible Li^+ insertion in organic electrolytes.[19]

To achieve good conformal electrodeposition of MnO_2 over a 3D porous conductive substrate, the latter must necessarily have a well-opened structure with accessible porosity to avoid any mass transport limitation of the soluble species involved in reaction 1. The approach also requires proper matching of the reactant concentrations and the conversion fluxes, which are linked to both the cycling rate and the specific area developed by the 3D conductive scaffold. In addition, due to the stoichiometry of the conversion process (4 equivalents of proton donor required, see reaction 1), strong pH gradients may be generated at the electrode/electrolyte interface, inducing the concomitant precipitation of insoluble phases such as zinc hydroxide sulfates (ZHS), as evidenced in several studies.[3,20–24] We believe this point contributes to the limited gravimetric capacities previously observed with unbuffered mild aqueous Zn/MnO_2 batteries.[4] To solve this issue, one strategy is to regulate the pH at the metal oxide/electrolyte interface, using a mild acidic buffered electrolyte at a sufficiently high concentration.[7]

In the present study, we demonstrate the decisive advantage of using a nanostructured current collector to fully exploit the reversible MnO_2-to-Mn^{2+} conversion from a buffered aqueous electrolyte containing Mn^{2+}. We also show that this conversion reaction remains highly efficient even in a Zn/MnO_2 battery cell configuration, which involves a Zn foil anode paired to the MnO_2 cathode and the presence of Zn^{2+} ions, in addition to Mn^{2+}, in the buffered electrolyte. For such purpose, we took advantage of 3D nanostructured indium-doped tin oxide (ITO) electrodes (1-μm-thick film deposited over a standard flat ITO-coated glass substrate) prepared by glancing angle deposition (GLAD), a technique which allows for the growth of metal oxides nanostructures in different shapes and morphologies.[25] These model mesoporous electrodes are characterized by a reproducible morphology with high aspect ratio and opened porosity,[26] well-suited for modification by electrodeposition as previously shown with conductive polymers.[27] In

addition, their transparency allows for *in-situ* UV-vis spectroelectrochemical monitoring, providing a real-time quantitative analysis of the amount of MnO_2 that electrodeposits/electrodissolves during the galvanostatic cycles.

Results and Discussion

The GLAD-ITO electrodes (1 μm-thick film) were prepared according to the published technique[25] using a deposition angle of 80° (see Experimental section) and rapid rotation. This combination leads to growth of vertically-oriented ITO nanopillars on an underlying commercial ITO substrate (Figure 1). The nanopillars are separated from one another with a void spacing in the range of tens of nanometers throughout the entire film thickness,[28] attesting to a well-opened mesoporosity.[29] An electroactive surface area enhancement of 45 was estimated from the capacitive current determined by cyclic voltammetry (CV) at different scan rates (see Supporting Information, Figure S1).

The pores of the GLAD-ITO electrodes were filled with MnO_2 by galvanostatic electrodeposition, controlling the amount of MnO_2 through the deposition time (see experimental section). The resulting MnO_2-modified electrodes were then characterized by SEM, XPS, EDX and UV-vis absorption spectroscopy as detailed in the Supporting Information. Cross-sectional SEM and EDX images reveal that MnO_2 uniformly grows inside the porosity of the GLAD structure and locally forms interwoven nanofibers (Figure 1). The top-view images in Figure 1 show that MnO_2 exhibits a typical carambola-like morphology, similar to that obtained from electrodeposited films on planar ITO electrodes. For the deposited charge of 240 $mC \cdot cm^{-2}$, the ITO nanocolumns remains clearly discernible from above (Figure 1), while at higher loads, once the pores of the GLAD ITO are filled, the MnO_2 deposit continues to develop far outside the

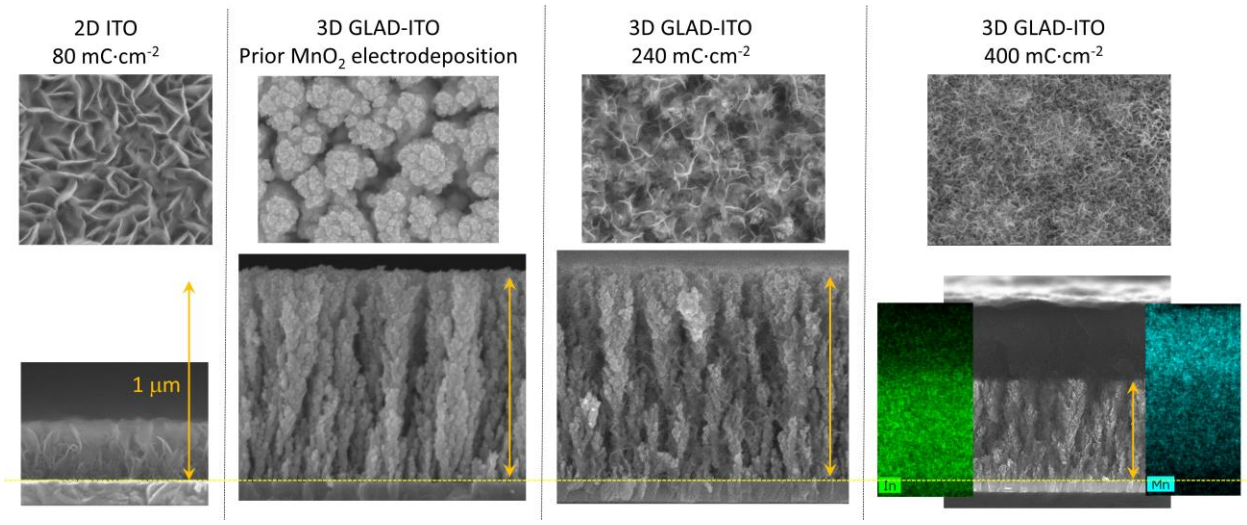

Figure 1 (2-columns). Top-view and cross-sectional SEM images of MnO_2 films electrodeposited on 2D ITO or 1 µm-thick GLAD-ITO electrodes, with different MnO_2 loads ranging from 0 to 400 mC·cm^{-2}. The orange arrow represents the 1 µm-bar scale. The dashed yellow lines delimit the planar ITO glass substrate underneath the MnO_2 film or the 3D GLAD-ITO structure. For the film loaded with 400 mC·cm^{-2} (rightmost images), the EDX mappings for In and Mn content are reported.

GLAD-ITO structure, making the ITO nanocolumns no longer discernable. This behavior is well evidenced in Figure 1, where a ~0.8 µm-thick MnO_2 film is observable by both SEM and spatially-resolved EDX on top of the GLAD-ITO electrode charged at 400 mC·cm^{-2} (an even thicker film, reaching ~1.6 µm, is observed for the electrode charged at 800 mC·cm^{-2}, see Figure S2D). Such a transition between filling of the GLAD-ITO pores with MnO_2 and subsequent growth far beyond the GLAD-ITO structure is also identified in the galvanostatic electrodeposition curves, showing after a certain delay a sudden ~20 mV jump in the potential. This potential jump is moreover linearly correlated with the GLAD-ITO thickness as the potential jump shifted from 150 to 90 and then 60 mC·cm^{-2} when the GLAD-ITO thickness decreased from 1 to 0.6 and then 0.3 µm, respectively (Figure S2A).

In order to investigate the benefit of a 3D nanostructured current collector on the reversible conversion of MnO_2 into Mn^{2+}, 1 µm-thick GLAD-ITO electrodes were loaded with an intermediate amount of deposited charge of 100 $mC \cdot cm^{-2}$ (or 48.4 $\mu g \cdot cm^{-2}$) to ensure the MnO_2 was fully restricted within the porous structure. The maximal capacity stored in these MnO_2-modifed electrodes was estimated from the average oxidation state (AOS) of the Mn centers, which in turn was determined from the linear correlation between the amount of electrodeposited Mn centers obtained by ICP quantification and the effective charge passed during the electrodeposition (see Supporting Information and Figure S2B for details). An AOS value of 3.86 was deduced, which is indicative of 1.86 electrons stored per Mn center. This value is in quite good agreement with the AOS of 3.75 determined by XPS analysis of the Mn(3s) peak splitting energy (Figure S2E). We thus conclude a maximal recoverable gravimetric capacity of 574 $mA \cdot h \cdot g^{-1}$ for the full conversion of the electrodeposited MnO_2, and we define the C-rate thanks to this value (1 C corresponding to 0.574 $A \cdot g^{-1}$).

MnO_2-GLAD-ITO electrodes charged at 100 $mC \cdot cm^{-2}$ were galvanostatically cycled in buffered electrolyte and concomitantly monitored by *in-situ* UV-vis spectroscopy. The results reported in Figure 2 demonstrate the full exploitation of MnO_2 when working in a 1 M acetate buffer at pH 5, containing 0.1 M $MnCl_2$. Indeed, full discharge of the capacity is reported with a near-perfect overlay of the first 20 galvanostatic cycles performed at 11 $A \cdot g^{-1}$ (19 C-rate), except for the initial discharge which is associated with a slightly lower capacity. Simultaneously, the electrode absorbance oscillates evenly and stably between 0.7 and 0, underlying the excellent reversibility of the MnO_2 electrodeposition/electrodissolution process. The absorbance value recorded at the end of each discharge cycle is close to the absorbance baseline (dashed line in Figure 2B), which demonstrates the complete reductive dissolution of MnO_2. The small and

stable voltage hysteresis (< 0.1 V) observed between the well-defined charge and discharge plateaus at rates lower than 11 $A \cdot g^{-1}$ is indicative of a rather fast reversible conversion process, occurring under nearly thermodynamic equilibrium (at least at rates < 11 $A \cdot g^{-1}$), as defined by the following Nernst equation:[7]

$$E = E^0_{MnO_2/Mn^{2+}} - 0.12 \times pH - 0.03 \times log(a_{Mn^{2+}}) \quad (2)$$

where $E^0_{MnO_2/Mn^{2+}}$is the standard potential of the MnO_2/Mn^{2+} redox coupled and $a_{Mn^{2+}}$ the activity of soluble Mn^{2+} ions. Hence, based on this equation, the highly stable charge and discharge potentials, leading to well-defined horizontal plateaus, suggest that no significant pH or Mn^{2+} gradients develop at the electrode/electrolyte interface within the range of rates investigated. The Coulombic efficiency reported in Figure 2F starts at 98% and rapidly tends to almost 100% after a few cycles, leading to an exceptionally high gravimetric capacity C_g of 560 ± 10 $mA \cdot h \cdot g^{-1}$ (see Experimental Section and SI for determination of C_g). This capacity, close to the aforementioned maximal capacity of 574 $mA \cdot h \cdot g^{-1}$, unambiguously demonstrates the full exploitation of the charge storage capacity that can be delivered by the present MnO_2-GLAD-ITO electrode. The excellent reversibility persists over long-term cycling: over 900 cycles at 44 $A \cdot g^{-1}$ (*i.e.*, 77 C), an almost constant Coulombic efficiency close to 100% is retained (*i.e.*, > 99.4 % for every cycle after the 5 initial cycles, see Figure 2D).

These results differ significantly from those obtained at 2D MnO_2-ITO electrodes, prepared by electrodeposition of MnO_2 on planar ITO electrodes with the same initial deposited charge of 100 $mC \cdot cm^{-2}$. Indeed, the data reported in Figure 2D demonstrate a significant accumulation of MnO_2 during the initial cycles, as attested by (*i*) the discharge capacities lower than 100 $mC \cdot cm^{-2}$, (*ii*) the CE < 90 %, and (*iii*) the nonzero absorbance value recorded at the end of each

discharge step. The fraction of MnO_2 accumulated after 20 cycles was roughly estimated from the absorbance value

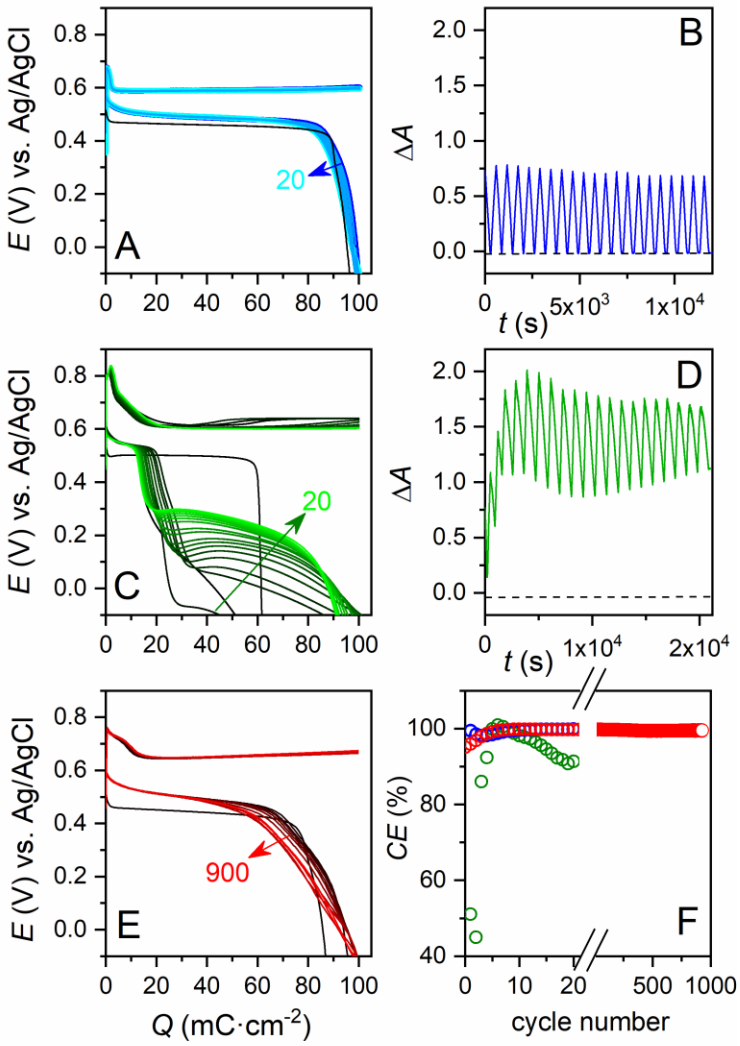

Figure 2 (1-column). Galvanostatic cycling of electrodes initially charged at 100 $mC \cdot cm^{-2}$ in a 1 M acetate buffer (pH 5) containing 0.1 M $MnCl_2$ and 0.85 M KCl. (A) Galvanostatic curves (20 cycles from dark to light blue with the first discharge in black) of a 3D MnO_2-GLAD-ITO electrode at 11 $A \cdot g^{-1}$ and (B) the corresponding UV-visible absorptometric traces. (C) Galvanostatic curves (20 cycles from dark to light green with the first discharge in black) of a 2D MnO_2-ITO electrode at 7.2 $A \cdot g^{-1}$ and (D) the corresponding UV-visible absorptometric traces (the black dashed line represents the absorbance baseline). (E) Galvanostatic curves recorded at a 3D MnO_2-GLAD-ITO electrode over 900 cycles at 44 $A \cdot g^{-1}$. Only the following

discharge/charge curves were overlayed: (black) initial discharge and (from dark red to light red) 1st, 10th, 20th, 50th, 100th, 200th, 300th, 500th, 700th and 900th cycles. (F) Evolution of the Coulombic efficiency as a function of the cycle number performed at a rate of: (green dots) 7.2 $A \cdot g^{-1}$ on a 2D MnO_2-ITO electrode, (blue dots) 11 and (red dots) 44 $A \cdot g^{-1}$ on a 3D MnO_2-GLAD-ITO electrode.

ΔA recorded at the end of the last cycle and corresponds to *ca.* 70 $\mu g \cdot cm^{-2}$ (see Supporting Information for details). This mass, equivalent to 145% of the mass electrodeposited during each charging step, indicates that only 40% of the MnO_2 is reversibly exploited. This leads to a significant loss in the gravimetric capacity, reaching only 235 $mA \cdot h \cdot g^{-1}$ after a few cycles. These observations are in line with what we previously reported at 2D MnO_2-ITO electrodes using the same electrolyte but with lower amounts of electrodeposited MnO_2.[7]

Another striking difference between the 3D MnO_2-GLAD-ITO and 2D MnO_2-ITO electrodes is the shape of the galvanostatic discharge curves, exhibiting one and two plateaus, respectively. At the MnO_2-GLAD-ITO electrode, the discharge potential centered on a well-defined value of 0.49 V is also remarkably stable until *ca.* 80% of the MnO_2 is electrodissolved. *On contrario*, the discharge curves recorded at the 2D MnO_2-ITO electrode exhibit, after a few cycles, a less well-defined supplementary plateau at a much lower potential of ~0.25V, corresponding to roughly 80 % of the total discharge process (Figure 2C). This shift in potential contributes to a huge increase in the voltage hysteresis, thereby severely affecting the charge storage energy efficiency. We previously attributed this second plateau to the formation of a more resistive fraction of MnO_2 at the planar electrode, a fraction which is probably much less electrically connected to the underlying current collector.[7] The lack of a second plateau with the 3D MnO_2-GLAD-ITO electrode tends to confirm this assumption. It also supports the idea that the 3D nanostructured substrate facilitates the electrical wiring of MnO_2 by shortening the electron transport distances

across the semi-conductive MnO_2. The nanostructuration effect relies on the good interpenetration between the conductive current collector and the semiconductive active material, wherein the restricted porous volume (characterized by small intercolomnar distances below 100 nm) restrains the thickness of MnO_2. Furthermore, we believe that the nanocolumns' roughness visible in SEM images (Figure 1) possibly increases the density of electrical contact points between MnO_2 and ITO. This result clearly highlights the benefit of the nanostructured electrode to facilitate the reversible electrodissolution/electrodeposition of MnO_2 into/from Mn^{2+}, and this benefit should persist as long as the conversion reaction remains within the porosity of the GLAD-ITO electrode. This latter assertion is corroborated by the cycling experiments in Figure S4, carried out with a progressive increase of the deposited charge from 100 up to 900 $mC \cdot cm^{-2}$ (*i.e.*, the amount of MnO_2 was increased until it grew far beyond the GLAD-ITO boundary). In the corresponding discharge curves, a second plateau at a lower potential of 0.3 V gradually emerged as the deposited charge increased. The development of this secondary plateau is also accompanied by a progressive and significant decrease in the Coulombic efficiency.

The efficiency and rate capability of the conversion process at MnO_2-GLAD-ITO electrodes was further investigated by cycling electrodes at different rates from 1.4 to 110 $A \cdot g^{-1}$ (*i.e.,* from 2.4 C to 190 C). The results gathered in Figure 3 first show that the Coulombic efficiency of the first cycles decreases as the rate increases, with initial CE values below 98% for rates > 22 $A \cdot g^{-1}$ (*i.e.* 38 C). Accordingly, a small fraction of poorly active MnO_2 accumulates at the electrode at the fastest rate during the early cycles, as attested by their lower CE value (see Figure 3C) and confirmed by the nonzero absorbance values ΔA recorded at the end of the discharge steps (Figure 3B). Therefore, avoiding fast rates early in the cycling provides sufficient time for nucleation and growth to proceed, thereby minimizing the early formation of the poorly active

fraction of MnO_2. The gravimetric capacities C_g of MnO_2-GLAD-ITO electrodes cycled at different rates are reported in Figure 3E. The data show that for rates < 11 $A \cdot g^{-1}$ (*i.e.*, < 19 C), the capacity remains almost constant at 560 ± 10 $mA \cdot h \cdot g^{-1}$ and close to the maximal value of 574 $mA \cdot h \cdot g^{-1}$, while at higher rates, the capacity decreases only slightly, remaining at 435 $mA \cdot h \cdot g^{-1}$ for 190 C. This remarkable result demonstrates the high rate capability of this conversion process, which is quite attractive for the development of sustainable high-power storage systems. It is worth noting that as the rate increases, the voltage hysteresis also gradually increases from 60 to 340 mV, with a limited ohmic drop contribution (estimated to be 30 Ω) which only represents 23 % of the total hysteresis at 190 C (Figure 3D). At the higher rates, we also notice an upward and downward drift of potential during the charging and discharging steps, respectively. Based on the Nernst equation (eq. 2), we assume this arises from local pH and/or Mn^{2+} gradient changes, driven by mass transport limitations. At the lower rates, while the overall discharge curves overlap, the small increase in the voltage hysteresis results mainly from an increase of the charging potential. This behavior suggests that electrodeposition is intrinsically a slower process than electrodissolution.

Overall, these results demonstrate that the combined use of a 3D nanostructured electrode with a mild acidic buffered electrolyte allows for full exploitation of an electrodeposited film of MnO_2. Such a combination is decisive to provide fast and reversible MnO_2-to-Mn^{2+} conversion, despite the multi-step mechanism, including proton-coupled electron transfer reactions as well as formation/breaking of metal-oxygen bonds.[30] The gravimetric capacity of 560 $mA \cdot h \cdot g^{-1}$ we report here at pH 5.0 is the highest yet reported in mild acidic electrolytes,[4] and remains competitive with the values recently achieved under much stronger acidic conditions (pH ~1).[9] Furthermore, the conversion reaction can be carried out at outstandingly high C-rates, competing

with the rate-performances achieved at MnO_2-based supercapacitors,[16] but with an incomparably greater charge storage capacity. Indeed, as illustrated in the Supporting Information, the present MnO_2-GLAD-ITO electrode in an unbuffered 1 M KCl electrolyte displayed a capacitance of 240 $F \cdot g^{-1}$, which is equivalent to 60 $mA \cdot h \cdot g^{-1}$ for a potential window of 0.9 V (Figure S3), *i.e.* ~9-times lower than in a buffered electrolyte.

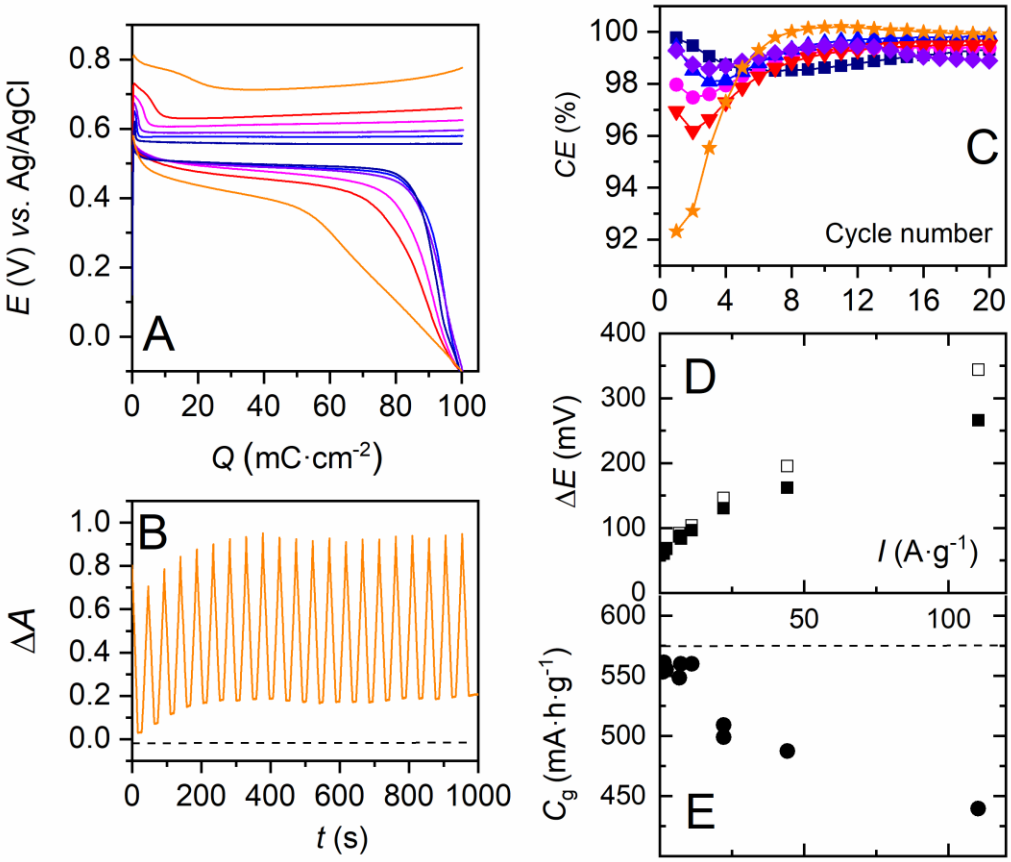

Figure 3 (1-column). Impact of the cycling rate over the galvanostatic cycling performances of MnO_2-GLAD-ITO electrodes (initial deposited charge: 100 $mC \cdot cm^{-2}$) in 1 M acetate buffer (pH 5) along with 0.1 M $MnCl_2$ and 0.85 M KCl. (A) 20th galvanostatic curves recorded respectively at (navy) 1.4, (blue) 7.2, (purple) 11, (pink) 22, (red) 44 and (orange) 110 $A \cdot g^{-1}$, and (B) the absorbance traces recorded during the 20 cycles performed at 110 A g^{-1}. (C) Coulombic efficiency as a function of the cycle number for different electrodes submitted to 20 galvanostatic cycles at a rate of: (navy) 1.4, (blue) 7.2, (purple) 11, (pink) 22, (red) 44 and (orange) 110 $A \cdot g^{-1}$. (D) Voltage hysteresis measured at half charge/discharge of the 20th cycle, monitored with (■)

and without (□) ohmic drop correction (30 Ω), and (E) gravimetric capacities inferred from the absorbance measurement of the 20th galvanostatic cycle determined at different rates for MnO_2-GLAD-ITO electrodes.

The 3D MnO_2-GLAD-ITO electrode was next assembled in the spectroelectrochemical cell with a Zn foil counter electrode to mimic a Zn/MnO_2 battery. The cell included an Ag/AgCl reference electrode to follow the potential of both MnO_2 and Zn electrodes while simultaneously monitoring the MnO_2 absorbance. Under these conditions, the following overall charge storage conversion reaction is expected:

$$MnO_{2(s)} + 4\ AH + Zn \leftrightarrows Zn^{2+}_{(aq)} + Mn^{2+}_{(aq)} + 4\ A^- + 2\ H_2O \qquad (3)$$

In addition to the acetate buffer (1.5 M, pH 5) and $MnCl_2$ (0.1 M), 0.25 M $ZnCl_2$ was added to the electrolyte, as required for the Zn-to-Zn^{2+} conversion reaction. The electrochemical performances of the Zn/MnO_2 assembly are given in Figure 4. An initial series of 20 galvanostatic cycles were recorded at an intermediate rate of 7.2 $A \cdot g^{-1}$ (referred here per gram of MnO_2). Well-defined single charge and discharge plateaus were observed at average potential values of 1.65 and 1.50 V *vs.* Zn^{2+}/Zn, respectively, which are very similar to those previously obtained in the Zn^{2+}-free electrolyte. The voltage hysteresis slightly increases by 60 mV upon cycling, but without significantly affecting the good energetic efficiency (*EE*), which remains higher than 86 % over the 20 cycles (blue dots in Figure 4F). Remarkably, after a few preconditioning cycles, the coulombic efficiency remains over 99 %, and from the residual absorbance of the cathode at the end of the discharge steps, we can conclude that only a very small amount of a less active fraction of MnO_2 accumulates, estimated to 6.5 $\mu g \cdot cm^{-2}$, and mainly arising within the first few cycles. Accordingly, the MnO_2 gravimetric capacity that can be fully exploited here is 500 $mAh \cdot g^{-1}$, slightly less than in the absence of Zn^{2+} but much higher than has previously been reported for mild aqueous Zn/MnO_2 batteries.[4] Finally, the long-term

cyclability of this aqueous Zn/MnO_2 cell configuration was confirmed through the near absence of capacity fading over 400 cycles at 20.6 $A \cdot g^{-1}$ (*i.e.*, 36 C, Figure 4E), with a Coulombic and an energetic efficiency that rapidly stabilize at 99.7 ± 0.2 % and 82.6 ± 1.3 %, respectively (red dots in Figure 4F). These results clearly

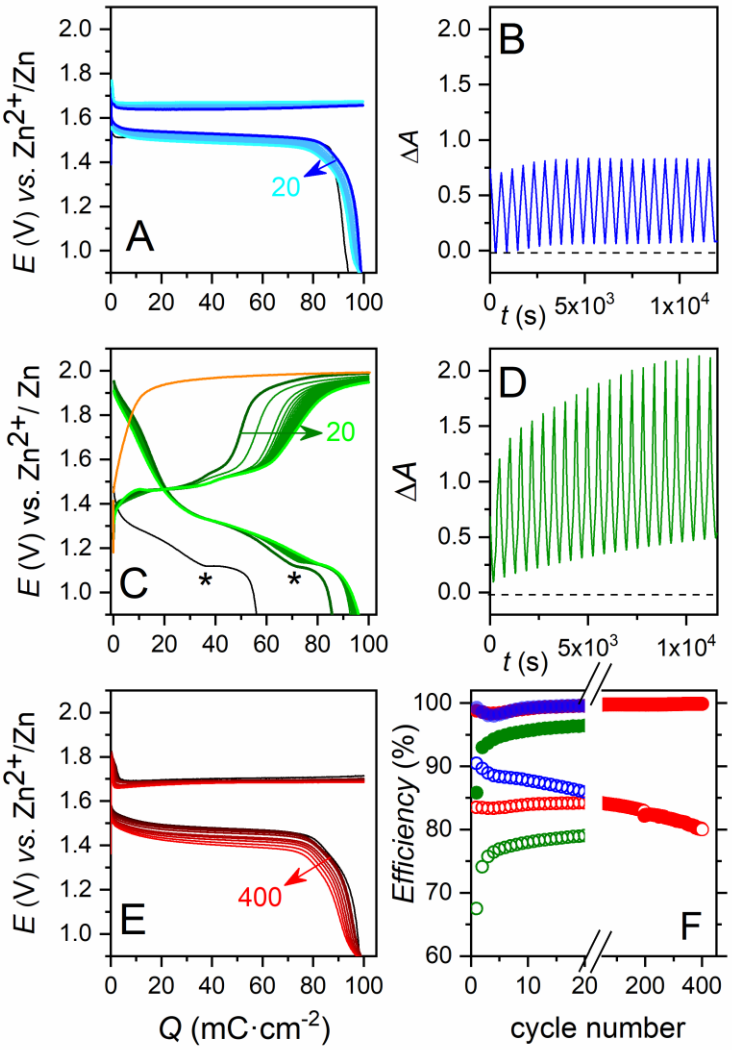

Figure 4 (1-column). Galvanostatic cycling performances of the Zn foil/MnO_2-GLAD-ITO assembly (initial charge 100 $mC \cdot cm^{-2}$) in pH 5 degassed electrolytes containing: (A, B, E) 1.5 M acetate buffer + 0.1 M $MnCl_2$ + 0.25 M $ZnCl_2$, and (C, D) 0.25 M $ZnCl_2$ + 0.1 M $MnCl_2$ + 0.85 M KCl. The potentiometric (A, C) and UV-visible absorptometric (B, D) traces were monitored concomitantly at a rate of 7.2 $A \cdot g^{-1}$ over 20 cycles with the initial discharge in black and the next

20 cycles from dark to light (either blue or green). (E) Galvanostatic curves recorded over 400 cycles at a rate of 20.6 $A \cdot g^{-1}$. Only the following discharge/charge curves were overlayed, from dark to light red: 1^{st}, 10^{th}, 20^{th}, 30^{th}, 50^{th}, 70^{th}, 100^{th}, 150^{th}, 200^{th}, 250^{th}, 300^{th}, 350^{th} and 400^{th} cycle. (F) Evolution of the (filled dots) Coulombic efficiency and (empty dots) energetic efficiency upon cycling the electrode at a rate of (green) 7.2 $A \cdot g^{-1}$ in the unbuffered electrolyte and (blue) 7.2 or (red) 20.6 $A \cdot g^{-1}$ in the buffered electrolyte.

demonstrate that the excellent performances of the MnO_2-GLAD-ITO electrodes are conserved in a Zn/MnO_2 assembly, and that the addition of Zn^{2+} in the buffered aqueous electrolyte does not significantly interfere with the reversible MnO_2-to-Mn^{2+} conversion reaction. This thus paves the way to the design of high-performance Zn/MnO_2 batteries in non-corrosive mild aqueous electrolytes.

In order to demonstrate the great benefit of using a buffered electrolyte in the aforementioned experiments, the Zn foil/MnO_2-GLAD-ITO assembly was cycled in an unbuffered aqueous electrolyte (adjusted to pH 5) containing only the inorganic salts required for the conversion reaction (*i.e.*, 0.1 M $MnCl_2$ and 0.25 M $ZnCl_2$ along with 0.85 M KCl). The electrochemical performances recorded at 7.2 $A \cdot g^{-1}$ are reported in Figure 4C. First, it is worth noting that both the Coulombic and the energetic efficiency are significantly deteriorated as compared to those previously obtained in a buffered electrolyte, remaining below 95 % and 79 %, respectively, over the 20 cycles (green dots in Figure 4F). Still, the reversible conversion mechanism is supported by the absorbance change monitored at the cathode, certifying the reversible electrodissolution/electrodeposition of MnO_2. The absorbance measurements also testify a significant accumulation of a less active form of MnO_2, estimated to be 37 $\mu g \cdot cm^{-2}$ after 20 cycles (*i.e.*, 76 % of the mass deposited during each charging step), leading to a significant loss in the MnO_2 exploitation and consequently to a lower gravimetric capacity of 310 $mA \cdot h \cdot g^{-1}$.

It is important to keep in mind that in the absence of acetate buffer, the available proton donors are the hexaaquo complexes $[Zn(H_2O)_6]^{2+}$ and $[Mn(H_2O)_6]^{2+}$ resulting from the solvation of their parent divalent inorganic salts (here $ZnCl_2$ and $MnCl_2$). These complexes are characterized by a weak Brønsted acidity with a pK_a value of 9.0 and 10.6, respectively.[31] As we previously demonstrated,[7] both complexes can act as proton donors to assist the electrodissolution of MnO_2 into Mn^{2+} according to the following electrochemical reaction:

$$MnO_{2(s)} + 4\ [M(H_2O)_6]^{2+} + 2\ e^- \leftrightarrows Mn^{2+}_{(aq)} + 4\ [M(H_2O)_5(OH)]^+ + 2\ H_2O \qquad (4)$$

where M is either Zn or Mn. This is typically what we observed in Figure 4C, where, after a few cycles, the galvanostatic discharges lead to a similar areal capacity than in the 1.5 M acetate buffer media, but with discharge curves of very different shapes. This striking difference can be rationalized through the pH-dependent Nernst eq. 2 associated with reaction 4. During the electrodissolution, protons brought by the hexaaquo complexes at the electrode/solution interface are rapidly consumed to ensure the conversion of MnO_2 into Mn^{2+}, resulting in the local production of the conjugated bases $[Zn(H_2O)_5OH]^+$ and $[Mn(H_2O)_5OH]^+$. Consequently, the local pH increases and the discharge potential decreases. Once the local pH is sufficiently basic, the doubly deprotonated neutral forms of $[Zn(H_2O)_6]^{2+}$ and $[Mn(H_2O)_6]^{2+}$ (*i.e.*, $Zn(OH)_2$ and $Mn(OH)_2$) precipitate, thereby stabilizing the local pH, an effect that is observed through the appearance of a stable plateau at the end of the discharge curves (the beginning of this plateau is indicated by an asterisk on Figure 4C).[24] Such precipitation of insoluble hydroxides over the MnO_2 cathode most likely contributes to a loss in the conversion efficiency, probably by slowing down the ongoing reductive dissolution of MnO_2. Evidence for the precipitation of such zinc hydroxides has been previously reported in several studies and also related to local pH changes.[3,20–24] However, none of these studies explicitly identified the proton source, preventing a clear explanation to the local pH changes and thus the associated precipitation of zinc

hydroxides, both governed by the pK_as and local activities of the weak acid and conjugated base acting as proton donor/acceptor.

Concerning the charging curves, which involve MnO_2 electrodeposition with the concomitant local release of several equivalents of protons, the first plateau observed at 1.45 V (Figure 4C) suggests a stabilization of the local pH at an intermediate mild acidic value. This effect can be rationalized from the dynamic equilibrium that is expected to persist through the continuous neutralization of the released protons by the Brønsted bases which are generated during the previous discharge step (and which include the precipitated hydroxides). This interpretation is further supported by the absence of a similar plateau when the galvanostatic charge is immediately applied to a MnO_2-GLAD-ITO electrode without prior discharge (orange curve, Figure 4C), leading to a direct rise of the charging potential up to a plateau at ~2 V *vs.* Zn^{2+}/Zn, which is close to the charging potential previously reported for an acidic Zn/MnO_2 battery (*i.e.*, 2.2 V in the presence of a 0.1 M H_2SO_4 electrolyte).[9] This result is thus indicative of the strong pH gradients that develop during the electrodeposition of MnO_2 from an unbuffered electrolyte.

Besides the demonstration of the beneficial effect of buffered electrolytes on the stabilization of the potentials of MnO_2 electrodeposition and electrodissolution, the present work also provides a clear explanation of the good performances recently achieved for a Zn/MnO_2 battery using an unbuffered aqueous electrolyte containing zinc and manganese acetate salts.[32] While the authors focus on the coordinating role of the acetate ions to explain the high performances they obtained and the low MnO_2 electrodeposition potential they observed (~1.8 V *vs*. Zn^{2+}/Zn), the present results rather suggest that the increased performance is due to a local buffering effect. Indeed, the protons locally released during the electrodeposition are neutralized by the acetate ions present in the electrolyte, generating acetic acid in dynamic equilibrium with the remaining

acetate ions. In the following discharge step, this acetic acid thus behaves as the proton donor to efficiently assist the reductive electrodissolution of MnO_2. It is worth noting that significant shifts of the charging and discharging potentials were reported in such unbuffered aqueous electrolytes, which most likely arises from significant variations in the local concentrations of acetate and acetic acid, and thus in the local pH.

Conclusion

In the present work, we demonstrate the beneficial combination of a nanostructured conductive substrate and a buffered electrolyte to fully exploit the reversible two-electron MnO_2-to-Mn^{2+} conversion mechanism in mild acidic conditions. The corresponding cathode is characterized by a high gravimetric capacity (560 $mA \cdot h \cdot g^{-1}$), high rate capability (435 $mA \cdot h \cdot g^{-1}$ at 190 C), low charge/discharge hysteresis (thus high energetic efficiency) and high cyclability (up to 900 cycles with a CE > 98%). Such performances are preserved in a Zn/MnO_2 cell configuration (*i.e.*, 500 $mA \cdot h \cdot g^{-1}$ at 12 C and a stable Coulombic efficiency of 99.7 % over 400 cycles at 36 C), outperforming all the mild aqueous Zn/MnO_2 assemblies so far described, with the additional advantage of a highly stable potential of 1.5 V over almost the complete discharge.

These great performances arise from properly balancing the electrolyte composition (to avoid mass transport limitation) and the MnO_2 mass loading regarding both the surface enhancement and the porosity of the nanostructured conductive 3D substrate (to avoid long-range electron transport throughout the semiconductive MnO_2 film and thus ohmic drop issues). The present demonstration was performed using transparent model GLAD-ITO electrodes, allowing for *in-situ* monitoring of the conversion process. These model electrodes, however, are unsuitable for charge storage applications, and therefore, further developments require scaling-up the conversion process with inexpensive, high surface area conductive substrates to get beyond the low gravimetric capacities of mild aqueous Zn/MnO_2 batteries.

Experimental Section

Chemicals. HNO_3 (Suprapur, 65%), acetic acid (Reagent plus, > 99%), KOH, HCl (Normapur, 37%), KCl (GR for analysis), ethanol absolute (EMSURE) and $ZnCl_2$ were purchased from Sigma-Aldrich/Merck. $MnCl_2$ tetrahydrate (99%) was purchased from Alfa Aesar. Acetone (Normapur) and chloroform (Normapur) were purchased from VWR Chemicals.

GLAD-ITO Mesoporous Electrodes. Porous ITO thin films were prepared by the glancing angle deposition (GLAD) method followed by thermal treatment as previously described.[25] Briefly, nanostructured ITO films were deposited from ITO evaporant (Cerac, 91:9 In_2O_3/SnO_2 99.99% pure) in an electron-beam physical vapor deposition system (Axxis, Kurt J Lesker) on ITO-coated glass substrates (8-12 Ω/□, Delta Technologies Ltd.). Throughout the deposition, substrates were maintained at an 80° angle with respect to impinging evaporant flux, while constantly rotating as a feedback-controlled function of the deposition rate. The film thickness was adjusted between 0.3 and 1 μm. Following deposition, the GLAD-ITO samples were thermally annealed in a two stage process, first under air at 500 °C and subsequently under 5% H_2/Ar flow at 375 °C, to improve and stabilize the optical and electrical properties. For such deposition conditions, the film porosity was previously estimated to be 0.5 and its density to be 4 $g \cdot cm^{-3}$.[25] Prior to the electrochemical experiments, the GLAD-ITO electrodes were cleaned by soaking them successively in chloroform, acetone, and ethanol, each time for 30 min at 50°C. After the electrodes were left to dry, a geometric area of 0.50 ± 0.04 cm^2 (N = 40) was delimited by depositing an insulating layer of nail polish.

Preparation of the MnO_2-coated GLAD-ITO electrodes. The deposition of MnO_2 within the 3D structure of GLAD-ITO electrodes was performed by galvanostatic electrodeposition

using a standard three-electrode cell configuration at room temperature (23 ± 3 °C) and a multichannel potentiostat/galvanostat (VSP model, BioLogic instrument). An SCE and Pt-grid were used as reference (+0.244 V *vs.* NHE) and counter electrode, respectively. For electrodeposition, freshly cleaned GLAD-ITO electrodes were placed in 7 mL of a quiescent acetate buffer (1 M, pH 5.0) containing 0.1 mM $MnCl_2$ and 0.85 M KCl. After preconditioning by cyclic voltammetry (CV) from 0.35 to 0.75 V (4 cycles) at 100 $mV \cdot s^{-1}$, galvanostatic electrodeposition at 300 $\mu A \cdot cm^{-2}$ (normalized to the geometric electrode area) was performed for a duration leading to final deposited charges, Q, ranging from 50 to 800 $mC \cdot cm^{-2}$. After electrodeposition, the MnO_2-modified electrodes were soaked for a few minutes in purified water and left to dry at room temperature. For each electrode, the initial amount of electrodeposited MnO_2 ($m^i_{MnO_2}$ in $\mu g \cdot cm^{-2}$) was estimated from the following relationship:

$$m^i_{MnO_2} = (0.484 \pm 0.008) \times Q \qquad (5)$$

Further details on the characterization of these MnO_2-coated GLAD-ITO electrodes by UV-visible absorption spectroscopy, XPS and ICP are reported in the Supporting Information.

Aqueous electrolyte compositions. Aqueous electrolytes with the following chemical composition were prepared in purified water: (*i*) 1 M acetate buffer (pK_a = 4.76) at pH 5.0 (prepared from a 2 M acetic acid solution adjusted to the desired pH with 2 M KOH) along with 0.1 M $MnCl_2$ and 0.85 M KCl (I = 1.9 M), (*ii*) 1.5 M acetate buffer at pH 5.0 along with 0.1 M $MnCl_2$ and 0.25 M $ZnCl_2$ (I = 2.3 M), (*iii*) 0.25 M $ZnCl_2$ along with 0.1 M $MnCl_2$ and 0.85 M KCl adjusted to pH 5.0 with 1 M HCl (I = 1.9 M), (*iv*) 1 M KCl adjusted to pH 5.0 with 1 M HCl (I = 1 M).

Spectroelectrochemistry. Spectroelectrochemical experiments were performed in a quartz UV-visible cell modified to accommodate three electrodes with an electrolyte volume of 1.2 mL.

The counter electrode was a Pt grid (0.06 mm wire diameter, 0.25 mm nominal space, Goodfellow) or a zinc foil (0.35 mm thickness, Goodfellow) and the reference electrode was a Dri-Ref Ag/AgCl/KCl_{sat} electrode (+0.2 V *vs*. NHE, WPI Instruments). Unless otherwise stated, all reported potentials are quoted against this reference electrode. The UV-visible absorption spectra were recorded in transmission mode using an HR-2000+ spectrometer (Ocean Optics) controlled by the SpectraSuite software. Spectra were obtained by averaging 50 individual spectra recorded with an integration time of 40 ms. For the galvanostatic experiments, the electrochemical cell was controlled by a VSP BioLogic potentiostat interfaced with the EC-Lab 11.3 software. A period of 10 s at the open circuit potential was systematically added at the end of each discharge during the galvanostatic cycling experiments to allow relaxation of the potential.

All gravimetric intensities ($A \cdot g^{-1}$) were calculated from the current density ($mA \cdot cm^{-2}$) applied to the electrode and the expected electrodeposited mass of MnO_2, deduced from eq. 5. The Coulombic efficiency (CE), energetic efficiency (EE), and gravimetric capacity (C_g in $mA \cdot h \cdot g^{-1}$) were calculated using the following equations:

$$CE = \frac{Q_{i,disch}}{Q_{i,ch}} \; ; \quad EE = \frac{E_{i,disch}}{E_{i,ch}} \; ; \quad C_g = \frac{1000}{3.6} \frac{Q_{i,disch}}{m_{ch}+m_{acc}} \qquad (6)$$

where $Q_{i,ch}$ and $Q_{i,disch}$ are the areal charging and discharging capacities of the i-th cycle in $mC \cdot cm^{-2}$, $E_{i,ch}$ and $E_{i,disch}$ the corresponding charging and discharging energy densities in $W \cdot h \cdot cm^{-2}$ determined from the product of Q and the average charge/discharge voltages, m_{ch} the areal MnO_2 mass deposited during the charging step (*i.e.*, 48.4 $\mu g \cdot cm^{-2}$ for a constant charge of 100 $mC \cdot cm^{-2}$), and m_{acc} the total areal inactive MnO_2 mass accumulated at the end of the experiment, determined from the absorbance of the electrode after the last discharge using eq. S2 and confirmed with ICP titration.

Film characterization. Scanning electron microscopy and energy dispersive x-ray spectroscopy were performed on a Hitachi S5500. XPS spectra were recorded using a K-Alpha+ system (ThermoFisher Scientific, East-Grinsted, UK) fitted with a micro-focused and monochromatic Al Kα X-ray source (1486.6 eV, spot size of 400 µm). The pass energy was set to 150 and 40 eV for the survey and the narrow high resolution regions, respectively. The spectra were calibrated against the (C—C/C—H) C(1s) component set at 285 eV. The chemical composition was determined using the manufacturer's sensitivity factors within the Avantage software (version 5.977). The average oxidation state (AOS) of the Mn centers in the electrodeposited MnO_2 thin-film was estimated on the basis of the XPS Mn(3s) peak splitting energy (ΔBE) and using the following correlation:[33,34]

$$AOS = 8.95 - 1.13 \times \Delta BE\ (eV) \qquad (7)$$

The amount of MnO_2 electrodeposited on ITO was analyzed by inductively coupled plasma atomic emission spectrometry (ICP-AES; Thermo Scientific iCAP 6300 ICP spectrometer) after dissolution of the MnO_2 film in concentrated nitric acid under ultrasonication and then dilution with purified water to have a final 6.5% v/v nitric acid concentration.

ASSOCIATED CONTENT

Supporting information

Elaboration and characterizations of the as-prepared MnO_2-GLAD-ITO electrodes (Galvanostatic curves, Absorbance and ICP quantification, XPS analysis and capacitive determination), Figures S1-S4.

AUTHOR INFORMATION

Corresponding Authors:

*E-mail: veronique.balland@u-paris.fr.

*E-mail: limoges@u-paris.fr

ORCID:

Véronique Balland: 0000-0001-9534-9659

Benoît Limoges: 0000-0002-2466-1896

Authors Contributions

The manuscript was written through contributions of all authors. All authors have given approval to the final version of the manuscript

Conflicts of interest

The authors declare no conflicts of interest.

Acknowledgements

The authors thank Gurvan Le Faucheur (U.F.R. de Chimie, Université de Paris) for ICP analysis, Philippe Decorse (ITODYS, CNRS, Université de Paris) for XPS measurements and Paul Concepcion (NRC, Edmonton, Canada) for SEM imaging and EDX analysis. We also gratefully acknowledge financial support from the French National Research Agency (ANR AqReBat project).

REFERENCES

(1) Larcher, D.; Tarascon, J. M. Towards Greener and More Sustainable Batteries for Electrical Energy Storage. *Nat. Chem.* **2015**, *7* (1), 19–29. https://doi.org/10.1038/nchem.2085.

(2) Huang, J.; Guo, Z.; Ma, Y.; Bin, D.; Wang, Y.; Xia, Y. Recent Progress of Rechargeable Batteries Using Mild Aqueous Electrolytes. *Small Methods* **2019**, *3* (1), 1–20. https://doi.org/10.1002/smtd.201800272.

(3) Pan, H.; Shao, Y.; Yan, P.; Cheng, Y.; Han, K. S.; Nie, Z.; Wang, C.; Yang, J.; Li, X.; Bhattacharya, P.; Mueller, K. T.; Liu, J. Reversible Aqueous Zinc/Manganese Oxide Energy Storage from Conversion Reactions. *Nat. Energy* **2016**, *1* (5), 16039. https://doi.org/10.1038/nenergy.2016.39.

(4) Fang, G.; Zhou, J.; Pan, A.; Liang, S. Recent Advances in Aqueous Zinc-Ion Batteries. *ACS Energy Lett.* **2018**, *3* (10), 2480–2501. https://doi.org/10.1021/acsenergylett.8b01426.

(5) Wu, B.; Zhang, G.; Yan, M.; Xiong, T.; He, P.; He, L.; Xu, X.; Mai, L. Graphene Scroll-Coated α-MnO_2 Nanowires as High-Performance Cathode Materials for Aqueous Zn-Ion Battery. *Small* **2018**, *14* (13), 1–8. https://doi.org/10.1002/smll.201703850.

(6) Xiong, T.; Yu, Z. G.; Wu, H.; Du, Y.; Xie, Q.; Chen, J.; Zhang, Y.-W. W.; Pennycook, S. J.; Lee, W. S. V.; Xue, J. Defect Engineering of Oxygen-Deficient Manganese Oxide to Achieve High-Performing Aqueous Zinc Ion Battery. *Adv. Energy Mater.* **2019**, *9* (14), 1803815. https://doi.org/10.1002/aenm.201803815.

(7) Mateos, M.; Makivic, N.; Kim, Y.-S.; Limoges, B.; Balland, V. Accessing the Two-Electron Charge Storage Capacity of MnO_2 in Mild Aqueous Electrolytes. *Adv. Energy Mater.* **2020**, 2000332. https://doi.org/10.1002/aenm.202000332.

(8) Pourbaix, M. *Atlas of Electrochemical Equilibria in Aqueous Solutions*, 2d English.; National Association of Corrosion Engineers, Houston, Texas, 1974.

(9) Chao, D.; Zhou, W.; Ye, C.; Zhang, Q.; Chen, Y.; Gu, L.; Davey, K.; Qiao, S. Z. An Electrolytic Zn–MnO_2 Battery for High-Voltage and Scalable Energy Storage. *Angew. Chemie - Int. Ed.* **2019**, 7823–7828. https://doi.org/10.1002/anie.201904174.

(10) Rolison, D. R.; Long, J. W.; Lytle, J. C.; Fischer, A. E.; Rhodes, C. P.; Mcevoy, T. M.; Bourg, E.; Lubers, A. M. Multifunctional 3D Nanoarchitectures for Energy Storage and Conversion. *Chem. Soc. Rev.* **2009**, *38* (1), 226–252. https://doi.org/10.1039/b801151f.

(11) Timmermans, M. Y.; Labyedh, N.; Mattelaer, F.; Zankowski, S. P.; Deheryan, S.; Detavernier, C.; Vereecken, P. M. Electrodeposition of Adherent Submicron to Micron Thick Manganese Dioxide Films with Optimized Current Collector Interface for 3D Li-Ion Electrodes. *J. Electrochem. Soc.* **2017**, *164* (14), 954–963. https://doi.org/10.1149/2.0091714jes.

(12) Zargouni, Y.; Deheryan, S.; Radisic, A.; Alouani, K.; Vereecken, P. M. Electrolytic Manganese Dioxide Coatings on High Aspect Ratio Micro-Pillar Arrays for 3D Thin Film Lithium Ion Batteries. *Nanomaterials* **2017**, *7* (126), 1–13. https://doi.org/10.3390/nano7060126.

(13) Guzman, R. N. De; Shen, A. A. Y.; Tian, T. Z. R.; Suib, S. L.; Ching, S. Electrical Resistivity

Measurements on Manganese Oxides with Layer and Tunnel Structures: Birnessites, Todorokites, and Cryptomelanes. *Chem. Mater.* **1995**, *7* (7), 1286–1292. https://doi.org/10.1021/cm00055a003.

(14) Le, M.; Liu, Y.; Wang, H.; Dutta, R. K.; Yan, W.; Hemminger, J. C.; Wu, R. Q.; Penner, R. M. In Situ Electrical Conductivity of Li_xMnO_2 Nanowires as a Function of x and Size. *Chem. Mater.* **2015**, *27*, 3494–3504. https://doi.org/10.1021/acs.chemmater.5b00912.

(15) Aricò, A. S.; Bruce, P.; Scrosati, B.; Tarascon, J.; Schalkwijk, W. V. A. N.; Picardie, U. De; Verne, J.; Umr-, C. Nanostructured Materials for Advanced Energy Conversion and Storage Devices. *Nat. Mater.* **2005**, *4* , 366–377.

(16) Huang, M.; Li, F.; Dong, F.; Zhang, Y. X.; Zhang, L. L. MnO_2 -Based Nanostructures for High-Performance Supercapacitors. *J. Mater. Chem. A* **2015**, *3* (43), 21380–21423. https://doi.org/10.1039/c5ta05523g.

(17) Cao, J.; Li, X.; Wang, Y.; Walsh, F. C.; Ouyang, J. Materials and Fabrication of Electrode Scaffolds for Deposition of MnO_2 and Their True Performance in Supercapacitors. *J. Power Sources* **2015**, *293*, 657–674. https://doi.org/10.1016/j.jpowsour.2015.05.115.

(18) Huang, Z. H.; Song, Y.; Feng, D. Y.; Sun, Z.; Sun, X.; Liu, X. X. High Mass Loading MnO_2 with Hierarchical Nanostructures for Supercapacitors. *ACS Nano* **2018**, *12* (4), 3557–3567. https://doi.org/10.1021/acsnano.8b00621.

(19) Zhang, H.; Yu, X.; Braun, P. V. Three-Dimensional Bicontinuous Ultrafast-Charge and -Discharge Bulk Battery Electrodes. *Nat. Nanotechnol.* **2011**, No. March, 1–5. https://doi.org/10.1038/nnano.2011.38.

(20) Kim, S. H.; Oh, S. M. Degradation Mechanism of Layered MnO_2 Cathodes in $Zn/ZnSO_4/MnO_2$ Rechargeable Cells. *J. Power Sources* **1998**, *72* (2), 150–158. https://doi.org/https://doi.org/10.1016/S0378-7753(97)02703-1.

(21) Lee, B.; Seo, H. R.; Lee, H. R.; Yoon, C. S.; Kim, J. H.; Chung, K. Y.; Cho, B. W.; Oh, S. H. Critical Role of PH Evolution of Electrolyte in the Reaction Mechanism for Rechargeable Zinc Batteries. *ChemSusChem* **2016**, *9* (20), 2948–2956. https://doi.org/10.1002/cssc.201600702.

(22) Chamoun, M.; Brant, W. R.; Tai, C. W.; Karlsson, G.; Noréus, D. Rechargeability of Aqueous Sulfate Zn/MnO_2 Batteries Enhanced by Accessible Mn^{2+} Ions. *Energy Storage Mater.* **2018**, *15* , 351–360. https://doi.org/10.1016/j.ensm.2018.06.019.

(23) Oberholzer, P.; Tervoort, E.; Bouzid, A.; Pasquarello, A.; Kundu, D. Oxide versus Nonoxide Cathode Materials for Aqueous Zn Batteries: An Insight into the Charge Storage Mechanism and Consequences Thereof. *ACS Appl. Mater. Interfaces* **2019**, *11* (1), 674–682. https://doi.org/10.1021/acsami.8b16284.

(24) Li, L.; Hoang, T. K. A.; Zhi, J.; Han, M.; Li, S.; Chen, P. Functioning Mechanism of the Secondary Aqueous Zn-β-MnO_2 Battery. *ACS Appl. Mater. Interfaces* **2020**, *12* (11), 12834–12846. https://doi.org/10.1021/acsami.9b22758.

(25) Krause, K. M.; Taschuk, M. T.; Harris, K. D.; Rider, D. A.; Wakefield, N. G.; Sit, J. C.; Buriak, J. M.; Thommes, M.; Brett, M. J. Surface Area Characterization of Obliquely Deposited Metal Oxide

Nanostructured Thin Films. *Langmuir* **2010**, *26* (6), 4368–4376. https://doi.org/10.1021/la903444e.

(26) Harris, K. D.; van Popta, A. C.; Sit, J. C.; Broer, D. J.; Brett, M. J. A Birefringent and Transparent Electrical Conductor. *Adv. Funct. Mater.* **2008**, *18* (15), 2147–2153. https://doi.org/10.1002/adfm.200800146.

(27) Rider, D. A.; Tucker, R. T.; Worfolk, B. J.; Krause, K. M.; Lalany, A.; Brett, M. J.; Buriak, J. M.; Harris, K. D. Indium Tin Oxide Nanopillar Electrodes in Polymer/Fullerene Solar Cells. *Nanotechnology* **2011**, *22* (8), 085706. https://doi.org/10.1088/0957-4484/22/8/085706.

(28) Renault, C.; Andrieux, C. P. C. P.; Tucker, R. T. R. T.; Brett, M. J. M. J.; Balland, V.; Limoges, B. Unraveling the Mechanism of Catalytic Reduction of O_2 by Microperoxidase-11 Adsorbed within a Transparent 3D-Nanoporous ITO Film. *J. Am. Chem. Soc.* **2012**, *134* (15), 6834–6845. https://doi.org/10.1021/ja301193s.

(29) Krause, K. M.; Vick, D. W.; Malac, M.; Brett, M. J. Taking a Little off the Top: Nanorod Array Morphology and Growth Studied by Focused Ion Beam Tomography. *Langmuir* **2010**, *26* (22), 17558–17567. https://doi.org/10.1021/la103070x.

(30) Huynh, M.; Bediako, D. K.; Liu, Y.; Nocera, D. G. Nucleation and Growth Mechanisms of an Electrodeposited Manganese Oxide Oxygen Evolution Catalyst. *J. Phys. Chem. C* **2014**, *118* (30), 17142–17152. https://doi.org/10.1021/jp501768n.

(31) Hawkes, S. J. All Positive Ions Give Acid Solutions in Water. *J. Chem. Educ.* **1996**, *73* (6), 516. https://doi.org/10.1021/ed073p516.

(32) Xie, C.; Li, T.; Deng, C.; Song, Y.; Zhang, H.; Li, X. A Highly Reversible Neutral Zinc/Manganese Battery for Stationary Energy Storage. *Energy Environ. Sci.* **2020**, *13*, 135–143. https://doi.org/10.1039/c9ee03702k.

(33) Galakhov, V. R.; Demeter, M.; Bartkowski, S.; Neumann, M.; Ovechkina, N. A.; Kurmaev, E. Z.; Lobachevskaya, N. I.; Mukovskii, Y. M.; Mitchell, J.; Ederer, D. L. Mn 3s Exchange Splitting in Mixed-Valence Manganites. *Phys. Rev. B - Condens. Matter Mater. Phys.* **2002**, *65* (11), 1–4. https://doi.org/10.1103/PhysRevB.65.113102.

(34) Sun, M.; Lan, B.; Lin, T.; Cheng, G.; Ye, F.; Yu, L.; Cheng, X.; Zheng, X. Controlled Synthesis of Nanostructured Manganese Oxide: Crystalline Evolution and Catalytic Activities. *CrystEngComm* **2013**, *15* (35), 7010–7018. https://doi.org/10.1039/c3ce40603b.

Table of Content – TOC illustration